

# Scavenging of Organic Pollutant And Fuel Generation Through Cost-Effective And Abundantly Accessible Rust: An Economical Approach For Waste Management And Energy Generation

**Nisar Khan**

Bacha Khan University Charsadda

**Idrees Khan**

Bacha Khan University Charsadda

**Tamanna Gul**

Bacha Khan University Charsadda

**Ibrahim Khan**

King Fahd University of Petroleum & Minerals

**Shahid Ali**

King Fahd University of Petroleum & Minerals

**Khalid Saeed** (✉ [khalidkhalil2002@yahoo.com](mailto:khalidkhalil2002@yahoo.com))

Bacha Khan University Charsadda

---

## Research Article

**Keywords:** Calcination, Rust, Photocatalyst, Photodegradation, Methylene blue, Water splitting

**Posted Date:** September 13th, 2021

**DOI:** <https://doi.org/10.21203/rs.3.rs-740375/v1>

**License:**  This work is licensed under a Creative Commons Attribution 4.0 International License.

[Read Full License](#)

---

# Abstract

At present, wastes management and energy generation are the foremost concerns due to their direct relationship with the biological species and environment. Herein we report utilization of iron rust (inorganic pollutant) as photocatalyst for photodegradation of methylene blue (MB) dye (organic pollutant) under visible light (economic) and water oxidation (energy generation). Iron rust was collected from metallic pipes and calcined in the furnace at 700 °C for 3 h in order to remove moisture/volatile content. The uncalcined and calcined Rust are characterized through scanning electron microscopy (SEM), energy dispersive spectroscopy (EDS), and Fourier transform infrared (FTIR) analysis, X-Ray Diffraction (XRD) and Thermogravimetric analysis (TGA). The morphological study illustrated that the shape of uncalcined and calcined iron rust is spongy, porous, and agglomerated. The XRD and DLS particle size is in a few hundred-nanometer range. The photodegradation (PD) investigation shows that calcined Rust is a potent photocatalyst for the PD of modeled MB and degraded about 94% in a very short time of 11 min. The photoelectrochemical (PEC) measurements revealed that calcined Rust is more active than uncalcined Rust under simulated 1-SUN illumination with respective photocurrent densities of  $\sim 0.40$  and  $\sim 0.32$  mA/cm<sup>2</sup>. These results demonstrate that cheaper and abundantly available Rust can be a useful candidate for environmental and energy applications.

## Introduction

Photocatalysis is a felicitous process and the most appropriate technology for the degradation of pollutants since it is cheap, reliable, efficient, and environmentally-friendly (Karthikeyan et al. 2020). Photocatalysis is based on semiconductor materials and is a promising, effective, and green technology for the removal of organic pollutants from aquatic environments (Yang et al. 2020; Costantino et al. 2020; Simon et al. 2020). Semiconductors are the most potential photocatalysts due to their appropriate bandgap energies and well-defined electronic configuration with occupied valence band and unoccupied conduction band (Cui et al. 2020). Photocatalysts are semiconductor solid oxides that can create electron-hole ( $e^-/h^+$  pairs) pairs upon absorption of light that react with the existing pollutants at the surface and oxidize them to less toxic substances (Saffari et al. 2020). Various semiconductor materials normally comprise such as TiO<sub>2</sub> (Sun et al. 2020; Pino et al. 2020), ZnO (Le et al. 2020), CuO (Khan et al. 2020), SnO<sub>2</sub> (Asaithambi et al. 2019), MnO<sub>2</sub> (Rahmat et al. 2019), WO<sub>3</sub> (Wang et al. 2019), CdS (Yu et al. 2020), NiO (Din et al. 2020),  $\alpha$ -Fe<sub>2</sub>O<sub>3</sub> (Sivula et al. 2010; Imran et al. 2020), etc. are explored as photocatalysts. However, most of these are either costly or prone to photocorrosion. Thus researchers are still examining the modified forms of these materials to find the best industrially feasible photocatalyst. Among these Fe<sub>2</sub>O<sub>3</sub> is considered as one of the favorable semiconductor photocatalysts due to its excellent stability, availability, cost, low bandgap (2.3 eV), and good harvesting capability of visible light. Additionally, low toxicity, environmental compatibility, and recyclability are the other attractive features of Fe<sub>2</sub>O<sub>3</sub> (Salgado and Valentini 2019; Lin et al. 2019; Ashraf et al. 2020). Fe<sub>2</sub>O<sub>3</sub> materials are utilized in many advanced fields like adsorption (Dehmani et al. 2020), solar cells (da Trindade et al. 2020), lithium-ion batteries (Xu et al. 2018), water splitting (Khan and Qurashi 2018;

Bouhjar et al. 2020; Makimizu et al. 2020) and dye degradation (Abhilash et al. 2019; Rincón Joya et al. 2019; Gupta et al. 2020). The production of nanoparticles through conventional methods such as hydrothermal, solgel, etc. requires more resources, time, energy, and human efforts, making the product expensive and limited product, which is a significant barrier from a commercial perspective (Dissanayake et al. 2019). Moreover, in some conventional syntheses, hazardous chemicals/precursors are employed, which is environmentally unfit (Karade et al. 2019). Hence, it is always desirable to develop an alternative, safe, and economical approach to synthesize the much-needed materials for various industrial applications.

In this work, we are able to devise a facile, safe, and economically feasible synthesis route to obtain the bulk amount of  $\text{Fe}_2\text{O}_3$ NPs from iron rust. A simple and straight forward treatment of rust results in high-quality  $\text{Fe}_2\text{O}_3$ NPs. Corrosion of metals is a constant and continuous problem and difficult to eliminate completely. The corrosion of ferrous metals in soil is a significant problem in oil and water storage tanks, transported pipelines, and cooling water pipeline distribution systems (Karthick et al. 2020). Current technologies are neither efficient to impede the corrosion ultimately nor effective in the recycling of waste iron rust (Babar et al. 2018). Herein, iron rust was not only converted into  $\text{Fe}_2\text{O}_3$ NPs but also utilized as a photocatalyst for the PD of MB dye in an aqueous medium and water splitting. Limited studies are reported on recycling and converting iron rust into catalysts such as  $\text{g-C}_3\text{N}_4\text{-Fe}_2\text{O}_3$  Photocatalyst (Babar et al. 2018),  $\text{LaFeO}_3$  Perovskite-Type Catalysts (Deganello et al. 2019),  $\text{Fe}_2\text{O}_3$  from toner powder (Gurav et al. 2020a). These methodologies mostly prepared composite type catalyst with hard and difficult preparation conditions which ultimately increase the process cost. The preparation conditions in these studies are time-consuming, not-scalable, and costly. Hence, the present study is not only economical in terms of photocatalyst preparation but also feasible to harvest visible light instead of hazardous and expensive UV-light.

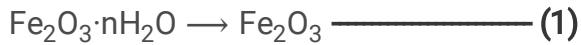
## Experimental Work

### 2.1 Materials

Iron rust was collected from water pipes of the local area (Lower Dir, KP, Pakistan). Nitric acid ( $\text{HNO}_3$ ) and sodium hydroxide ( $\text{NaOH}$ ) were provided by Sigma Aldrich. Methylene blue dye was purchased from Scharlau Chemicals.

### 2.2 Preparation of photocatalyst

The collected iron rust was first washed with distilled  $\text{H}_2\text{O}$  to remove any attached impurities and then dried in an oven at  $130^\circ\text{C}$  for 5 h. The dried Rust was calcined at  $700^\circ\text{C}$  for 3 h to remove the adhered moisture content. The high temperature removes the attached water molecules from the iron rust ( $\text{Fe}_2\text{O}_3 \cdot n\text{H}_2\text{O}$ ) and convertsthem into  $\text{Fe}_2\text{O}_3$  NPs as can be seen in Eq. 1. After calcination, the sample was cooled in a desiccator and then packed in order to avoid moistening.



## 2.3 Photodegradation study of Methylene blue dye

The  $\text{Fe}_2\text{O}_3$  NPs were utilized as photocatalyst for the PD of MB dye under visible light in an aqueous solution as a function of different operational parameters e.g., irradiation time, photocatalyst reusability, catalyst amount, and initial dye concentration. In time study, 0.02g (2g/L) of the photocatalyst was added to 10 mL solution of MB dye (15 ppm) and sonicated for 2 min for complete dispersion of NPs. The sample was then kept in dark to attain adsorption-desorption equilibrium. The sample was then kept under standard light with constant and continuous stirring for different irradiation times (1, 3, 5, 7, 9, and 11 min). After the reaction time completion, the photocatalyst was separated through centrifugation (12000 rpm for 10 min).

The %degradation of MB dye is calculated from the following formulas:

$$\text{Degradation (\%)} = \left( \frac{C_0 - C}{C_0} \right) \times 100 \quad (\text{a})$$

$$\text{Degradation (\%)} = \left( \frac{A_0 - A}{A_0} \right) \times 100 \quad (\text{b})$$

Where  $C_0$  represents the initial concentration of dye,  $C$  stands for dye concentration after the reaction,  $A_0$  symbolizes initial absorbance, and  $A$  shows the absorbance of dye after the reaction.

## 2.4 Photoelectrode fabrication and Photoelectrochemical measurements

PEC water splitting of uncalcined and calcined Rust was performed in a three-electrode PEC cell containing 0.5 M  $\text{Na}_2\text{SO}_4$  (Sigma Aldrich) electrolyte (pH 7.2). The uncalcined and calcined Rust deposited FTOs were used as the working electrodes and were controlled by an Autolab potentiostat. Platinum (Pt) and saturated calomel electrode (SCE) served as the counter and reference electrodes, respectively. For the preparation of the working electrode, we have dissolved 2 mg of the photocatalyst in 2mL DI water. Which is sonicated for 30 mins, followed by the addition of one drop of 5% Nafion (as a binder). The dispersed solution is drop casted over  $0.25 \text{ mm}^2$  conducting glass (fluorinated tin oxide). All PEC measurements were recorded using NOVA software installed on a data collecting device under the controlled chopping of dark and light. A solar simulator (Oriel Sol-3A Newport) provided artificial solar light irradiation and the power was calibrated using a silicon diode solar cell (Oriel-diode) and fixed at  $100 \text{ mW/cm}^2$ , which is equivalent to 1 SUN. The solar simulator was also equipped with AM-1.5 G and UV cutoff ( $\lambda > 420 \text{ nm}$ ) filters.

## 2.5 Morphological, Structural and Optical Characterizations

The synthesized  $\text{Fe}_2\text{O}_3$  NPs were characterized through Fe-SEM and EDX (LA-6490, JEOL Japan, in the energy range of 0–20 keV). Each sample was prepared from the dry sample in ethanol followed by

sonication for 30 minutes. The FT-IR analysis was carried out via FT-IR (Nicolet Nexus 470, Thermo Electron Co., USA). The photodegradation study was performed by UV-Visible spectrophotometer (Model = Shimadzu 1800, Japan). Dynamic light scattering (particle size distribution and zeta potential). X-ray diffraction (XRD) was carried out using Rigaku Miniflex II Desktop X-ray diffractometer for  $2\theta$  range of 5–80°, sampling step size of 0.03° and 3.00 scan speed. The particle size of the synthesized materials was measured by Zetasizer nano Series dynamics light scattering (DLS = ZEN3600, Malvern, UK). All the samples were sonicated before each run for 15 minutes by a probe sonicator (UP400St, Hielscher, Germany) in ethanol. The surface area was analyzed by a Micromeritics ASAP 2020 BET analyzer. Initially, the samples were degassed at 180°C for 4 h under a vacuum to eliminate impurities, prior to N<sub>2</sub> physisorption measurements. The TGA analysis was performed by using Mettler Toledo analyser (TGA/SDTA-851e, Switzerland) under nitrogen environment, with temperature from 25 to 800 °C at the scan rate of 10 °C/min to determine the thermal properties of calcined and uncalcined samples.

## Results And Discussion

### 3.1 Morphological, Elemental and Mapping analysis

SEM analysis is a powerful tool to study surface morphological features of the photocatalyst. Figure 1(a-d) represents the lower and higher magnification SEM micrographs of the as-collected uncalcined and calcined iron rust, respectively. After comparing the morphologies, it is clear that both samples are showing significant agglomerations, with highly irregular morphologies. Moreover, SEM micrographs indicate that the individual particle sizes in both cases are in the nanometer range, which agglomerated into large blocks of irregular shape particles. We assume that other parameters could promote the photo- and photoelectrocatalytic performance of calcined Rust compare to uncalcined Rust, under similar conditions. Therefore, we have characterized these samples further with XRD, BET, and TGA to confirm those parameters, which are contributing to enhanced catalytic performance.

Figures 2 and 3 illustrated the elemental analysis and mapping study of uncalcined and calcined Rust, respectively. Figures 2a show the EDX spectra of uncalcined Rust with %elemental composition in tabular form. The representing peaks for Fe, C, Zn, Si, Al, and O are observed with respective %compositions of each element. As expected, the %compositions indicate that the Fe and O are present in higher concentration compared to Zn, Si, and Al, which are existed in minuscule quantities. The presence of Zn, Si, and Al elements can be justified as the Rust was collected from a steel source, that contains these metals in proportions (to enhance their strength). Figure 2b-d presented the mapping results of Fe, O, and Si, respectively. The mapping study revealed the presence of Si, which is due to earthy impurities as Rust is obtained from the ground water pipes. Figure 3 represents the EDX spectra and % elemental composition (tabular form) of calcined iron rust, displaying peaks for C, Zn, K, Si, Ca, Al and O. The percentage of Fe and O were found higher than other elements. Furthermore, the percentage of oxygen in the case of calcined Rust is lower than uncalcined Rust NPs, which might be due to the elimination of any attached water and other volatile matter. The quantity of C is also reduced after calcination due to its

oxidation to CO<sub>2</sub>. Moreover, in the case of calcined Rust, we have observed K and Ca in trace amounts, which could be possibly added from the ceramics where we have calcined the Rust at a high temperature, i.e. 700 °C. Figure 3b-d presented the mapping results of Fe, O, and Si, respectively. It is essential to state that we deliberately not removed the various elemental impurities to see their overall effect on photocatalysis and also to look after the high cost.

## 3.2 Structural analysis of uncalcined and calcined Rust

FT-IR spectroscopy is known for its high sensitivity, especially in the detection of inorganic and organic species with low content. Figure 4 shows the FT-IR spectra of uncalcined and calcined Rust representing various peaks in different regions. The uncalcined Rust NPs show peaks at about 1033cm<sup>-1</sup>, which might be due to the lepidocrocite (ferric mineral) (Veneranda et al. 2018). The peaks at about 903 and 799 cm<sup>-1</sup> might be due to the goethite (hydrated iron oxide) (S and A 1993). The absorption peak in the absorption band of uncalcined Rust at 1630 cm<sup>-1</sup> is the characteristic peak of -OH, indicating a large amount of crystal water in the corrosion products (Wang et al. 2020). This peak almost disappears in the calcined Rust due to high-temperature calcination. Similarly, the calcined iron rust NPs also gives peaks at about 1033, and 903 and 799 cm<sup>-1</sup>, which might be due to the lepidocrocite and goethite, respectively. The spectrum of calcined iron rust also presented prominent peaks at about 526 and 436 cm<sup>-1</sup> is due to the stretching vibration of Fe-O (Rahim et al. 2011).

The chemical composition, phase purity, and crystallinity of the uncalcined and calcined were identified via XRD analysis. The XRD patterns of the uncalcined and calcined iron rust are shown in Fig. 5a. The XRD pattern of the uncalcined rust clearly indicates that this contains a mixture of FeOOH and iron oxide (γ-Fe<sub>2</sub>O<sub>3</sub>). On the other hand, the XRD pattern of the calcined rust shows diffraction peaks balanced at 30.18°, 57.28°, and 62.94° corresponding to the (220), (511) and (440) planes of γ-Fe<sub>2</sub>O<sub>3</sub> iron (JCPDS file nos. 75 – 1594). The peaks located at 24.26°, 33.17°, 40.82°, and 49.57° match well with the (012), (104), (113), and (024) planes of α-Fe<sub>2</sub>O<sub>3</sub> (JCPDS file no. 33 – 0664). This means that calcined rust is the combination of γ-Fe<sub>2</sub>O<sub>3</sub> and α-Fe<sub>2</sub>O<sub>3</sub> iron. The quantification of XRD patterns indicates that the sample contains ~ 75% α-Fe<sub>2</sub>O<sub>3</sub> and ~ 25% γ-Fe<sub>2</sub>O<sub>3</sub>. The crystallite particle size is also calculated from XRD patterns by a widely reported Debye-Scherrer equation as below (Salavati-Niasari et al. 2008; Khan et al. 2017).

$$D = \frac{K\lambda}{(\beta \cos \theta)} \quad (c)$$

Where D is showing the crystallite size (nm), K is crystallite shape factor, approximated to be 0.9, λ is x-ray wavelength, β is full width at half the maximum (FWHM) in radians and θ is Bragg's angle. By averaging the values of all peaks, the crystallite size of the calcined rust was about 374.5 nm, which is less than the uncalcined sample. The calcination temperature is efficient for the phase transformation of thermodynamically unstable iron oxides to Fe<sub>2</sub>O<sub>3</sub> phase by losing water molecule (Sarif et al. 2020; Ashraf et al. 2020; Gurav et al. 2020b). To further see the effect of calcination on the particle size we also

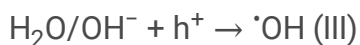
performed the DLS analysis. The DLS particle size distribution of uncalcined and calcined rust is represented in Fig. 5b. The uncalcined rust has a broad peak representing its agglomeration and the average particle size of uncalcined was found to be as high as ~ 487 nm. Comparatively, the calcine rust sample demonstrates a significantly sharp peak area, which indicates a sharp particle distribution. The calculated average particle size of the calcined sample is measured to be ~ 379 nm. These XRD and DLS results indicate that the calcination reduced the particle size significantly, which can add incremental characteristics to the photocatalytic behavior of rust. Dehydration and phase conversion due to calcination at high temperature cause a decrease in attractive forces thus the dispersed and displayed small particle size than uncalcined rust. Thermogravimetric analysis (TGA) measurements of both samples were carried out to find their thermal stability and the results are represented in Fig. 5c. The isotherms indicate the uncalcined iron rust lost about 21 % weight loss at a maximum temperature of 800°C. The attached and adsorbed water is removed at above 120°C. Maximum weight loss occurs between 200 to 300 °, however, no significant weight loss is observed above 500°C. In the case of calcined rust, only 2 % weight was lost during its thermal analysis, which is showing the thermostable nature of calcined samples as their calcination is already performed at a high temperature of 700°C. Finally, the effect of calcination over the surface area is also performed through the Brunauer-Emmett-Teller (BET) adsorption method with nitrogen gas (Fig. 5d). It can be seen in Fig. 5d, that both isotherms are of type IV. The calcination increased the specific surface area (SSA) of calcined rust to 98.84 m<sup>2</sup>/g, which was 29.30 for an uncalcined sample. The three times enhancement in the SSA indicated that after calcination the crystallization and phase transformation took place, which also reduces the particle size as indicated by the XRD and DLS results.

### 3.3 Photodegradation of Methylene blue

The obtained Fe<sub>2</sub>O<sub>3</sub>·nH<sub>2</sub>O and prepared Fe<sub>2</sub>O<sub>3</sub> NPs were utilized as photocatalysts for the PD of MB dye in an aqueous medium under visible light. Figure 6a represents the UV-Vis spectra of MB dye before reaction and after different visible light reaction time in the presence of calcined Fe<sub>2</sub>O<sub>3</sub> NPs, displaying that dye degradation increase with increasing irradiation time. Figure 6b shows the %degradation of MB dye in the presence of Fe<sub>2</sub>O<sub>3</sub>·nH<sub>2</sub>O, Fe<sub>2</sub>O<sub>3</sub> NPs, and without photocatalysts (photolysis). Without photocatalyst, and in the presence of Fe<sub>2</sub>O<sub>3</sub>·nH<sub>2</sub>O no considerable degradation was observed while Fe<sub>2</sub>O<sub>3</sub> NPs significantly degraded MB dye in a short time. The uncalcined Rust have little adsorption capability and thus display less photocatalytic efficiency. The increased photocatalytic efficiency of Fe<sub>2</sub>O<sub>3</sub> NPs than Fe<sub>2</sub>O<sub>3</sub>·nH<sub>2</sub>O is due to its high-temperature calcination, which makes the materials porous and ultimately adsorb the dye efficiently followed by drastic PD. It was reported that calcination enhances catalysts activity (Al-Fatesh and Fakeeha 2012). The result shows that Fe<sub>2</sub>O<sub>3</sub> NPs rapidly degraded 82.5% dye within 1 min and then beyond this time a small increase observed in the efficiency of PD, and finally degraded about 94% dye within 11 min. Initially, the degradation efficiency is much faster and slows down upon increasing the irradiation time. This is because at the beginning formation of •OH radicals is faster and the more availability of the active site for dye adsorption. After a particular reaction time, the remaining active site is not easy to fill because of the repulsive force between the molecules on the

surface with the bulk phase, and thus after sometime the %degradation tends to be constant (Aziztyana et al. 2019). The sustainability of Fe<sub>2</sub>O<sub>3</sub> NPs is evaluated by utilizing recovered and re-recovered Fe<sub>2</sub>O<sub>3</sub> NPs under the same experimental conditions. The photocatalyst was recovered by washing with distilled water and oven drying at 100°C. Figure 6c represents the comparison of %degradation of MB dye PD by fresh, recovered, and re-recovered Fe<sub>2</sub>O<sub>3</sub> NPs. The results revealed that the fresh Fe<sub>2</sub>O<sub>3</sub> NPs (1st run) degraded about 94% MB dye within 11 min, while the recovered (2nd run) and re-recovered (3rd ) run degraded about 71.7% and 62% dye, respectively within the same irradiation time. The decrease observed in the photocatalytic activity of the recycled photocatalysts might be due to the blockage of active surface sites by deposition of the photo insensitive hydroxides (Khan et al. 2019).

The photodegradation of MB dye occurs as visible light adsorbed by Fe<sub>2</sub>O<sub>3</sub> NPs that result in excitation of electrons (e<sup>-</sup>) from valence band (VB) to the conduction band (CB), creating positively charged holes (h<sup>+</sup>) in the valence band. The hole in the VB reacts with H<sub>2</sub>O molecules and produces hydroxyl radicals (<sup>•</sup>OH), while the e<sup>-</sup> present in the CB reacts with an oxygen molecule and produces superoxide anion radical (<sup>•</sup>O<sub>2</sub><sup>-</sup>). These generated radicals are highly reactive and degraded MB dye molecules into intermediates products and finally into more unaffected species such as CO<sub>2</sub> and H<sub>2</sub>O as shown in Fig. 7. The possible reaction steps in this mechanism are summarized in the following equations (Khan et al. 2019).



The effect of pH on the PD of MB was also evaluated as various discharge their effluents at different pH. Figure 8a shows the effect of pH of the medium on the photodegradation efficiency of MB dye keeping irradiation time (1 min) and initial dye concentration (15 ppm) constant. It was observed that the efficiency of photodegradation of MB is much faster in the basic medium as compared to the acidic medium. It might be due that in the basic medium the photocatalysts tend to acquire a negative charge that results in increased adsorption of positively charged MB (cationic) dyes because of the rising electrostatic attraction (Nguyen Thi Thu et al. 2016). The Figure revealed that from acidic medium to pH 8 the degradation efficiency is almost constant and then enormously increased at pH 9. The results confirmed that at pH 3 the Fe<sub>2</sub>O<sub>3</sub> NPs degraded about 54% dye which increases to 95% by increasing the pH of the medium to 9. Similarly, the effect of photocatalyst dosage and initial dye concentration was also evaluated, and the results are represented in Figs. 8b,c, respectively. Figure 8b represents that efficiency of photodegradation increases rapidly by increasing Fe<sub>2</sub>O<sub>3</sub> NPs dosage up to a specific limit (optimum amount) and then level off beyond that limit. The results verified that till 0.02g photocatalyst

dose, the PD is rapidly increasing and a maximum of 82.5% MB dye degraded in 1 mi. However, further dose increments showed very little enhancement in the PD performance of the photocatalyst. At 0.035g catalyst dose, the PD efficiency increases to ~ 93% within the same time. The leveling in PD with increasing catalyst dosage might be the increase in solution opacity which decreases the penetration of the photon flux and ultimately decreases the photocatalytic degradation efficiency (Khan et al. 2020). The effect of initial MB dye concentration is consolidated in Fig. 8c, displaying that maximum PD is achieved at a lower concentration. According to the results, a maximum PD of 92% occurs at an initial concentration of 5 ppm, which frequently decreases to 72.9% by increasing dye concentration to 25 ppm. Such decreases in PD with increasing dye concentration are due to the more adsorption of dye molecules on the catalyst surface and occupy its active sites. The adsorb dye molecules absorb a significant amount of light rather than a catalyst which decrease the generation of hydroxyl radical and hence reduces the photocatalytic efficiency (Reza et al. 2017).

Production of H<sub>2</sub> attracts attention because it is essential for fuel and chemical reactions(Yamada et al. 2020). Both calcined and uncalcined were also utilized for water splitting. The PEC performance of the calcined and uncalcined rust photoelectrodes was explored via chronoamperometry and linear-sweep voltammetry (LSV). Figure 9a,b indicates the dosing effect on the overall water oxidation for calcined and uncalcined photoanodes. It can be seen that increasing the catalyst dose from 0.1 to 0.3 mg/50mL ethanol has a nonsignificant effect in the case of uncalcined samples. However, the calcined samples indicate enhancement in the activity until 0.3 mg/50mL ethanol, after which saturation took place and no further photocurrent density enhancement observed. Figure 9c displays the LSV measurements under regular solar illumination. For both the samples, the photocurrent remained significantly lower under dark, while under the simulated light, the photocurrent densities increased enormously beyond 0.7 V vs RHE with the voltage sweep, as indicated by the I-V spectra. The spectra represent that both the materials are photoactive, but the photocurrent density of calcined Rust ( $0.42 \text{ mA cm}^{-2}$ ) is much higher than uncalcined Rust ( $0.34 \text{ mA cm}^{-2}$ ), which can be attributed to the good crystallinity and porosity of the calcined sample. A significant dark current appeared above 1.23 V vs RHE for the calcined rust photoelectrodes, which can be attributed to electrochemical processes (Khan and Qurashi 2017). The photocurrent densities observed at the thermodynamic potential (1.23 Vvs RHE) of the water oxidation reaction were ~ 0.40 and ~ 0.32 mA/cm<sup>2</sup> for calcined and uncalcined, respectively. Moreover, it is important to sate the onset potential of calcined rust shift cathodically to 0.96 V vs RHE from 1.07 V vs RHE (for uncalcined sample). The excellent photodegradation efficiency, photostability, and photocurrent density, with good cathodic onset potential shift of calcined Rust, indicate that it could be a feasible photocatalytic as well as photoelectrocatalytic materials for future energy and environment applications. Figure 9d shows the long-term I-t photostability curve obtained from photoanodes under the light with an illumination period of 80 min under calibrated simulated 1-SUN power. The results revealed that the stability curve of calcined Rust decreased insignificantly and showed small photocorrosion decay and hence offered considerable resilience and stability during the irradiation period. Similarly, the stability curve of uncalcined Rust significantly decreased with more considerable photocorrosion decay, which can be attributed to the photocorrosion of this material due to structural faults and charge high

recombination rate. The uncalcined rust lost its PEC activity entirely after 57 min, due to uncontrolled photodecay.

The optoelectrical characteristics are useful to realize the photoactivity of the samples. For this purpose, we have performed the UV/Vis-diffuse reflectance analysis of the powder sample. The samples were measured using a quartz cell, from wavelength ranges from 200 to 800 nm at the scan rate of 50 nm/min. As indicated in Fig. 9e, the calcined samples are showing superb enhancement in the visible light absorption. The onset value of absorption in the range of 580–600 nm for the calcined sample indicates that the bandgap value is well in the order of visible light region and suitable for PEC water splitting application. The samples are expected to show improved Photocatalytic water splitting and dye degradation performance, which is the case as discussed above. To further support over claim we also measured the resistivity and surface transport behavior of the samples via electronic impedance spectroscopy (EIS) measured at 0.2 V vs. SCE under AM 1.5 G irradiation as shown in the Fig. 9f. Based on the semicircle diameter of the Nyquist plots one can realize the interfacial charge transport behavior (Khan and Qurashi 2018; Khan et al. 2021). The larger the semicircle means lower the transportation and vice versa. By comparing the circles it can be concluded that the calcined rust sample has more interfacial transport than the uncalcined. This means that the generated electrons/holes are facilely transferred in case of calcined rust, hence minimizing the charge recombination and enhance the over all photo and photlectrocatalytic activity. A comparison table (Table 1) is also provided which is showing some existing hemtite based materials with their photocurrent denisties and photostabilities.

Table 1  
Photocurrent densities and photostability of some reported hematite based photoanodes

S/No	Materials	Photocurrent density@1.23 vs. RHE	Photostability density@1.23 vs. RHE	Ref.
1	$\alpha\text{-Fe}_2\text{O}_3/\text{TiO}_2$	1.05 mA/cm <sup>2</sup>	2500 s	(Khan and Qurashi 2018)
	Ag/ $\alpha\text{-Fe}_2\text{O}_3/\text{TiO}_2$	2.59 mA/cm <sup>2</sup>	3600 s	
2	$\text{Fe}_2\text{O}_3$	1.55 mA/cm <sup>2</sup>	—	(Wei et al. 2020)
	FeOOH/ $\text{Fe}_2\text{O}_3$	2.40 mA/cm <sup>2</sup>	5 h	
3	Ta: $\text{Fe}_2\text{O}_3@Fe_2O_3$	2.45 mA/cm <sup>2</sup>	5 h	(Zhang et al. 2020)
	NiFe(OH) <sub>x</sub> /Ta: $\text{Fe}_2\text{O}_3@Fe_2O_3$	3.22 mA/cm <sup>2</sup>	5 h	
4	$\text{Fe}_2\text{O}_3$	0.12 mA/cm <sup>2</sup>	2 h	(Tang et al. 2019)
	$\text{Fe}_2\text{O}_3/\text{Fe}_2\text{TiO}_5$	0.90 mA/cm <sup>2</sup>	2 h	
	$\text{Fe}_2\text{O}_3/\text{Fe}_2\text{TiO}_5/\text{CoFe-PBA}$	1.25 mA/cm <sup>2</sup>	2 h	
5	Uncalcined rust	0.34 mA cm <sup>-2</sup>	20 min	This work
	Calcined rust	0.42 mA cm <sup>-2</sup>	70 min	This work

## Conclusion

Calcination of Rust is an economical and straightforward way for efficient  $\text{Fe}_2\text{O}_3$  NPs photocatalysts preparation. Calcined Rust is a novel, economic and efficient photocatalyst for the PD of MB dye in aqueous medium and water oxidation under visible light. The enhanced photocatalytic efficiency of calcined to uncalcined rust is due to its high-temperature calcination, which makes the materials porous and perform efficient adsorption of dye followed by PD. The  $\text{Fe}_2\text{O}_3$  NPs are highly sustainable and can be used several times. The enhanced PD in the basic medium is due to more generation of hydroxyl radical in alkaline medium. The efficiency of PD increases incrementally with photocatalyst dosage and a decrease in initial dye concentration. The enhanced PEC water oxidation activity of calcined Rust might be due to its porous structure via high-temperature calcination, which facilitates the light absorption and provides a sufficient pathway for carrier transport, hence suppressing the charge recombination.

## Declarations

**Funding:** Not applicable.

**Authors' contributions:** All authors contribute equally in the writing and compilation and finalizing the article.

**Competing interests:** The authors declare that they have no competing interests.

**Availability of data and materials:** Not applicable.

### **Ethical Approval and Consent to Participate**

Not applicable

### **Consent to Publish**

Not applicable

### **Authors Contributions**

1. Nisar Khan: Performed all the experimental work in the current study
2. Idrees Khan: Helped during the photodegradation study and helped to Analyzed the samples
3. Tamanna Gul: Helped during the catalysts preparation and performed the study of recycled catalysts in the current study.
4. Ibrahim Khan: Utilized the catalysts as economical photocatalyst for water splitting to produce H<sub>2</sub> fuel.
5. Shahid Ali: Performed the characterized the samples
6. Khalid Saeed: Given the main Idea and supervised all work

### **Funding**

Bacha Khan University Charsadda supported the current study

### **Competing Interests**

The authors declare that they have no competing interests

### **Availability of data and materials**

Not applicable

## **References**

1. Abhilash MR, Akshatha G, Srikantaswamy S (2019) Photocatalytic dye degradation and biological activities of the Fe<sub>2</sub>O<sub>3</sub>/Cu<sub>2</sub>O nanocomposite. RSC Adv 9:8557–8568.

<https://doi.org/10.1039/c8ra09929d>

2. Al-Fatesh ASA, Fakeeha AH (2012) Effects of calcination and activation temperature on dry reforming catalysts. *J Saudi Chem Soc* 16:55–61. <https://doi.org/10.1016/j.jscs.2010.10.020>
3. Asaithambi S, Sakthivel P, Karuppaiah M et al (2019) Preparation of SnO<sub>2</sub> Nanoparticles with Addition of Co Ions for Photocatalytic Activity of Brilliant Green Dye Degradation. *J Electron Mater* 48:2183–2194. <https://doi.org/10.1007/s11664-019-07061-5>
4. Ashraf M, Khan I, Usman M et al (2020) Hematite and Magnetite Nanostructures for Green and Sustainable Energy Harnessing and Environmental Pollution Control: A Review. *Chem Res Toxicol*. <https://doi.org/10.1021/acs.chemrestox.9b00308>
5. Aziztyana AP, Wardhani S, Prananto YP et al (2019) Optimisation of Methyl Orange Photodegradation Using TiO<sub>2</sub>-Zeolite Photocatalyst and H<sub>2</sub>O<sub>2</sub> in Acid Condition. In: IOP Conference Series: Materials Science and Engineering. Institute of Physics Publishing, p 042047
6. Babar S, Gavade N, Shinde H et al (2018) Evolution of Waste Iron Rust into Magnetically Separable g-C<sub>3</sub>N<sub>4</sub>-Fe<sub>2</sub>O<sub>3</sub> Photocatalyst: An Efficient and Economical Waste Management Approach. *ACS Appl Nano Mater* 1:4682–4694. <https://doi.org/10.1021/acsanm.8b00936>
7. Bouhjar F, Derbali L, Marí B, Bessaïs B (2020) Electrodeposited chromium-doped  $\alpha$ -Fe<sub>2</sub>O<sub>3</sub> under various applied potential configurations for solar water splitting. *Results Phys* 102996. <https://doi.org/10.1016/j.rinp.2020.102996>
8. Costantino F, Armirotti A, Carzino R et al (2020) In situ formation of SnO<sub>2</sub> nanoparticles on cellulose acetate fibrous membranes for the photocatalytic degradation of organic dyes. *J Photochem Photobiol A Chem* 398:112599. <https://doi.org/10.1016/j.jphotochem.2020.112599>
9. Cui Y, Peng L, Lei L et al (2020) Synthesis and Photocatalytic Performance of Superparamagnetic Fe-Ag@AgCl Nanowire with 1-D Core–Shell Structure under Visible Light. *J Photochem Photobiol A Chem* 397:112586. <https://doi.org/10.1016/j.jphotochem.2020.112586>
10. da Trindade LG, Hata GY, Souza JC et al (2020) Preparation and characterization of hematite nanoparticles-decorated zinc oxide particles (ZnO/Fe<sub>2</sub>O<sub>3</sub>) as photoelectrodes for solar cell applications. *J Mater Sci* 55:2923–2936. <https://doi.org/10.1007/s10853-019-04135-x>
11. Deganello F, Joshi M, Liotta LF et al (2019) Sustainable Recycling of Insoluble Rust Waste for the Synthesis of Iron-Containing Perovskite-Type Catalysts. *ACS Omega* 4:6997–7004. <https://doi.org/10.1021/acsomega.8b03522>
12. Dehmani Y, Alrashdi AA, Lgaz H et al (2020) Removal of phenol from aqueous solution by adsorption onto hematite ( $\alpha$ -Fe<sub>2</sub>O<sub>3</sub>): Mechanism exploration from both experimental and theoretical studies. *Arab J Chem* 13:5474–5486. <https://doi.org/10.1016/j.arabjc.2020.03.026>
13. Din MI, Tariq M, Hussain Z, Khalid R (2020) Single step green synthesis of nickel and nickel oxide nanoparticles from *Hordeum vulgare* for photocatalytic degradation of methylene blue dye. *Inorg Nano-Metal Chem* 50:292–297. <https://doi.org/10.1080/24701556.2019.1711401>
14. Dissanayake DMSN, Mantilaka MMMGPG, Palihawadana TC et al (2019) Facile and low-cost synthesis of pure hematite ( $\alpha$ -Fe<sub>2</sub>O<sub>3</sub>) nanoparticles from naturally occurring laterites and their

- superior adsorption capability towards acid-dyes. RSC Adv 9:21249–21257.  
<https://doi.org/10.1039/c9ra03756j>
15. Gupta NK, Ghaffari Y, Bae J, Kim KS (2020) Synthesis of coral-like  $\alpha$ -Fe<sub>2</sub>O<sub>3</sub> nanoparticles for dye degradation at neutral pH. J Mol Liq 301:112473. <https://doi.org/10.1016/j.molliq.2020.112473>
  16. Gurav R, Surve SK, Babar S et al (2020a) Rust-derived Fe<sub>2</sub>O<sub>3</sub> nanoparticles as a green catalyst for the one-pot synthesis of hydrazinyl thiazole derivatives. Org Biomol Chem. <https://doi.org/10.1039/d0ob00109k>
  17. Gurav R, Surve SK, Babar S et al (2020b) Rust-derived Fe<sub>2</sub>O<sub>3</sub> nanoparticles as a green catalyst for the one-pot synthesis of hydrazinyl thiazole derivatives. Org Biomol Chem 18:4575–4582. <https://doi.org/10.1039/d0ob00109k>
  18. Imran M, Abutaleb A, Ashraf Ali M et al (2020) UV light enabled photocatalytic activity of  $\alpha$ -Fe<sub>2</sub>O<sub>3</sub> nanoparticles synthesized via phase transformation. Mater Lett 258:126748. <https://doi.org/10.1016/j.matlet.2019.126748>
  19. Karade VC, Parit SB, Dawkar VV et al (2019) A green approach for the synthesis of  $\alpha$ -Fe<sub>2</sub>O<sub>3</sub> nanoparticles from Gardenia resinifera plant and its In vitro hyperthermia application. Heliyon 5:e02044. <https://doi.org/10.1016/j.heliyon.2019.e02044>
  20. Karthick S, Muralidharan S, Saraswathy V (2020) Corrosion performance of mild steel and galvanized iron in clay soil environment. Arab J Chem 13:3301–3318. <https://doi.org/10.1016/j.arabjc.2018.11.005>
  21. Karthikeyan C, Arunachalam P, Ramachandran K et al (2020) Recent advances in semiconductor metal oxides with enhanced methods for solar photocatalytic applications. J Alloys Compd 828:154281
  22. Khan I, Ali S, Mansha M, Qurashi A (2017) Sonochemical assisted hydrothermal synthesis of pseudo-flower shaped Bismuth vanadate (BiVO<sub>4</sub>) and their solar-driven water splitting application. Ultrason Sonochem 36:386–392. <https://doi.org/10.1016/J.ULTSONCH.2016.12.014>
  23. Khan I, Baig N, Ali S et al (2021) Progress in layered cathode and anode nanoarchitectures for charge storage devices: Challenges and future perspective. Energy Storage Mater 35:443–469
  24. Khan I, Khan I, Usman M et al (2020) Nanoclay-mediated photocatalytic activity enhancement of copper oxide nanoparticles for enhanced methyl orange photodegradation. J Mater Sci Mater Electron 1–15. <https://doi.org/10.1007/s10854-020-03431-6>
  25. Khan I, Qurashi A (2018) Sonochemical-Assisted In Situ Electrochemical Synthesis of Ag/ $\alpha$ -Fe<sub>2</sub>O<sub>3</sub>/TiO<sub>2</sub> Nanoarrays to Harness Energy from Photoelectrochemical Water Splitting. ACS Sustain Chem Eng 6:11235–11245. <https://doi.org/10.1021/acssuschemeng.7b02848>
  26. Khan I, Qurashi A (2017) Shape Controlled Synthesis of Copper Vanadate Platelet Nanostructures, Their Optical Band Edges, and Solar-Driven Water Splitting Properties. Sci Rep 7:1–11. <https://doi.org/10.1038/s41598-017-14111-7>
  27. Khan I, Sadiq M, Khan I, Saeed K (2019) Manganese dioxide nanoparticles/activated carbon composite as efficient UV and visible-light photocatalyst. Environ Sci Pollut Res 26:5140–5154.

<https://doi.org/10.1007/s11356-018-4055-y>

28. Le TK, Nguyen TMT, Nguyen HTP et al (2020) Enhanced photocatalytic activity of ZnO nanoparticles by surface modification with KF using thermal shock method. Arab J Chem 13:1032–1039. <https://doi.org/10.1016/j.arabjc.2017.09.006>
29. Lin Z, Du C, Yan B, Yang G (2019) Amorphous Fe<sub>2</sub>O<sub>3</sub> for photocatalytic hydrogen evolution. Catal Sci Technol 9:5582–5592. <https://doi.org/10.1039/c9cy01621j>
30. Makimizu Y, Nguyen NT, Tucek J et al (2020) Activation of  $\alpha$ -Fe<sub>2</sub>O<sub>3</sub> for Photoelectrochemical Water Splitting Strongly Enhanced by Low Temperature Annealing in Low Oxygen Containing Ambient. Chem – A Eur J 26:2685–2692. <https://doi.org/10.1002/chem.201904430>
31. Nguyen Thi Thu T, Nguyen Thi N, Tran Quang V et al (2016) Synthesis, characterisation, and effect of pH on degradation of dyes of copper-doped TiO<sub>2</sub>. J Exp Nanosci 11:226–238. <https://doi.org/10.1080/17458080.2015.1053541>
32. Pino E, Calderón C, Herrera F et al (2020) Photocatalytic Degradation of Aqueous Rhodamine 6G Using Supported TiO<sub>2</sub> Catalysts. A Model for the Removal of Organic Contaminants From Aqueous Samples. Front Chem 8:365. <https://doi.org/10.3389/fchem.2020.00365>
33. Rahim AA, Kassim MJ, Rocca E, Steinmetz J (2011) Mangrove (Rhizophora apiculata) tannins: An eco-friendly rust converter. Corros Eng Sci Technol 46:425–431. <https://doi.org/10.1179/174327809X457003>
34. Rahmat M, Rehman A, Rahmat S et al (2019) Highly efficient removal of crystal violet dye from water by MnO<sub>2</sub> based nanofibrous mesh/photocatalytic process. J Mater Res Technol 8:5149–5159. <https://doi.org/10.1016/j.jmrt.2019.08.038>
35. Reza KM, Kurny A, Gulshan F (2017) Parameters affecting the photocatalytic degradation of dyes using TiO<sub>2</sub>: a review. Appl Water Sci 7:1569–1578. <https://doi.org/10.1007/s13201-015-0367-y>
36. Rincón Joya M, Barba Ortega J, Malafatti JOD, Paris EC (2019) Evaluation of Photocatalytic Activity in Water Pollutants and Cytotoxic Response of  $\alpha$ -Fe<sub>2</sub>O<sub>3</sub> Nanoparticles. ACS Omega 4:17477–17486. <https://doi.org/10.1021/acsomega.9b02251>
37. S N, A R (1993) The application of infrared spectroscopy to the study of rust systems-II. Study of cation deficiency in magnetite(Fe<sub>3</sub>O<sub>4</sub>) produced during its transformation to maghemite( $\gamma$ -Fe<sub>2</sub>O<sub>3</sub>) and hematite( $\alpha$ -Fe<sub>2</sub>O<sub>3</sub>). Corros Sci 34:1355–1365
38. Saffari R, Shariatnia Z, Jourshabani M (2020) Synthesis and photocatalytic degradation activities of phosphorus containing ZnO microparticles under visible light irradiation for water treatment applications. Environ Pollut 259:113902. <https://doi.org/10.1016/j.envpol.2019.113902>
39. Salavati-Niasari M, Davar F, Mir N (2008) Synthesis and characterization of metallic copper nanoparticles via thermal decomposition. Polyhedron 27:3514–3518. <https://doi.org/10.1016/j.poly.2008.08.020>
40. Salgado BCB, Valentini A (2019) Evaluation of the photocatalytic activity of SiO<sub>2</sub>@TiO<sub>2</sub> hybrid spheres in the degradation of methylene blue and hydroxylation of benzene: Kinetic and mechanistic

- study. *Brazilian J Chem Eng* 36:1501–1518. <https://doi.org/10.1590/0104-6632.20190364s20190139>
41. Sarif M, Hilgert J, Khan I et al (2020) Selective Synthesis of Monodisperse CoO Nanooctahedra as Catalysts for Electrochemical Water Oxidation. *Langmuir* 36:21. <https://doi.org/10.1021/acs.langmuir.0c02131>
  42. Simon YDT, Hadis B, Estella TN et al (2020) Urea and green tea like precursors for the preparation of g-C<sub>3</sub>N<sub>4</sub> based carbon nanomaterials (CNMs) composites as photocatalysts for photodegradation of pollutants under UV light irradiation. *J Photochem Photobiol A Chem* 398:112596. <https://doi.org/10.1016/j.jphotochem.2020.112596>
  43. Sivula K, Zboril R, Le Formal F et al (2010) Photoelectrochemical Water Splitting with Mesoporous Hematite Prepared by a Solution-Based Colloidal Approach. *J Am Chem Soc* 132:7436–7444. <https://doi.org/10.1021/ja101564f>
  44. Sun Q, Li K, Wu S et al (2020) Remarkable improvement of TiO<sub>2</sub> for dye photocatalytic degradation by a facile post-treatment. *New J Chem* 44:1942–1952. <https://doi.org/10.1039/c9nj05120a>
  45. Tang P, Han L, Hegner FS et al (2019) Boosting Photoelectrochemical Water Oxidation of Hematite in Acidic Electrolytes by Surface State Modification. *Adv Energy Mater* 9:1901836. <https://doi.org/10.1002/aenm.201901836>
  46. Veneranda M, Aramendia J, Bellot-Gurlet L et al (2018) FTIR spectroscopic semi-quantification of iron phases: A new method to evaluate the protection ability index (PAI) of archaeological artefacts corrosion systems. *Corros Sci* 133:68–77. <https://doi.org/10.1016/j.corosci.2018.01.016>
  47. Wang L, Hu H, Xu J et al (2019) WO<sub>3</sub> nanocubes: Hydrothermal synthesis, growth mechanism, and photocatalytic performance. *J Mater Res* 34:2955–2963. <https://doi.org/10.1557/jmr.2019.189>
  48. Wang Z, Wang M, Jiang J et al (2020) Atmospheric Corrosion Analysis and Rust Evolution Research of Q235 Carbon Steel at Different Exposure Stages in Chengdu Atmospheric Environment of China. *Scanning* 2020:. <https://doi.org/10.1155/2020/9591516>
  49. Wei Y, Liao A, Wang L et al (2020) Room temperature surface modification of ultrathin FeOOH cocatalysts on Fe<sub>2</sub>O<sub>3</sub> photoanodes for high photoelectrochemical water splitting. *J Nanomater* 2020:. <https://doi.org/10.1155/2020/7148714>
  50. Xu L, Tian Y, Liu T et al (2018) α-Fe<sub>2</sub>O<sub>3</sub> nanoplates with superior electrochemical performance for lithium-ion batteries. *Green Energy Environ* 3:156–162. <https://doi.org/10.1016/j.gee.2018.01.005>
  51. Yamada T, Suzuki N, Nakata K et al (2020) Hydrogen Production System by Light-Induced α-FeOOH Coupled with Photoreduction. *Chem – A Eur J* 26:2380–2385. <https://doi.org/10.1002/chem.201903642>
  52. Yang J, Liu Z, Wang Y, Tang X (2020) Construction of a rod-like Bi<sub>2</sub>O<sub>4</sub> modified porous g-C<sub>3</sub>N<sub>4</sub> nanosheets heterojunction photocatalyst for the degradation of tetracycline. *New J Chem*. <https://doi.org/10.1039/D0NJ01922D>
  53. Yu Z, Qian L, Zhong T et al (2020) Enhanced visible light photocatalytic activity of CdS through controllable self-assembly compositing with ZIF-67. *Mol Catal* 485:110797.

<https://doi.org/10.1016/j.mcat.2020.110797>

54. Zhang H, Li D, Byun WJ et al (2020) Gradient tantalum-doped hematite homojunction photoanode improves both photocurrents and turn-on voltage for solar water splitting. Nat Commun 11.: <https://doi.org/10.1038/s41467-020-18484-8>

## Figures

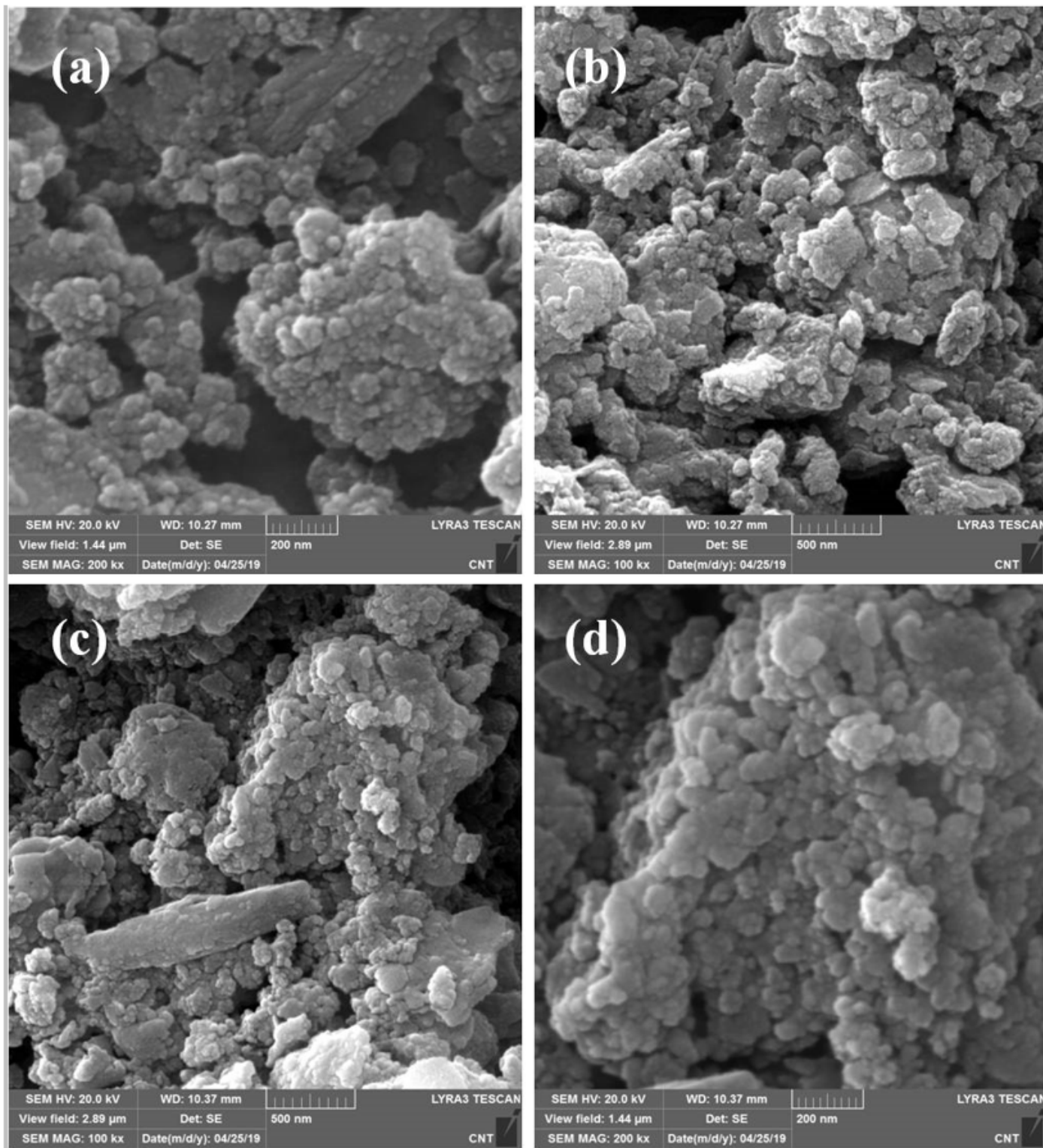


Figure 1

SEM images of (a, b) Uncalcined iron rust (c, d) Calcined rust

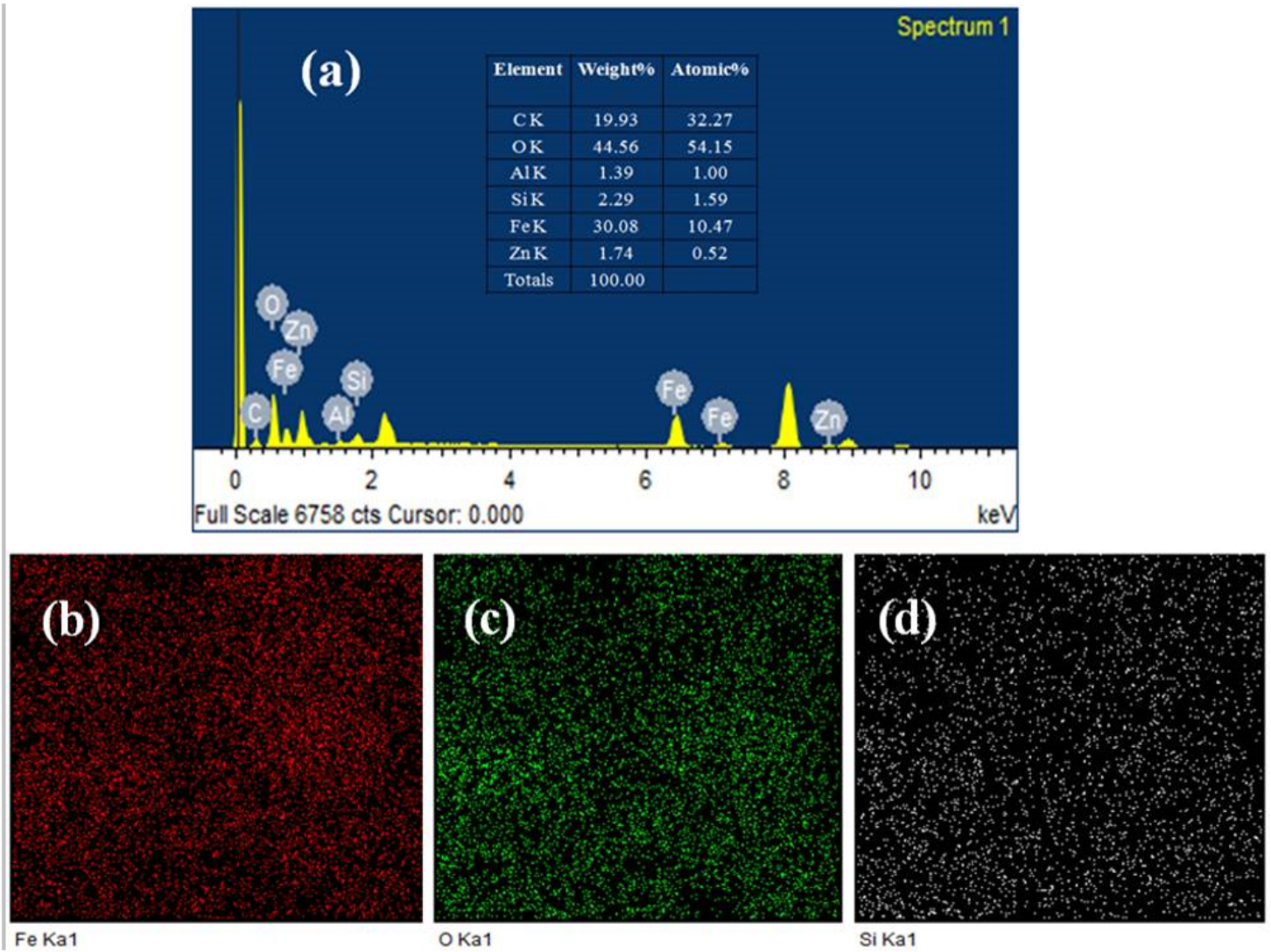
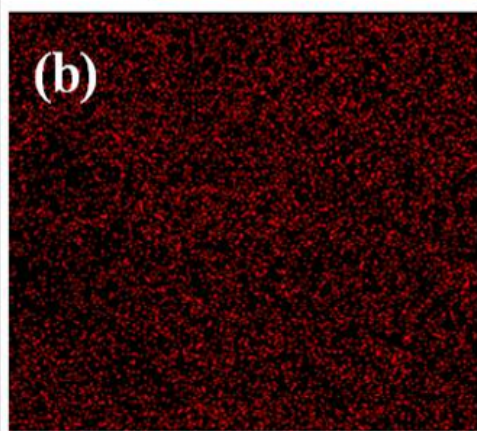
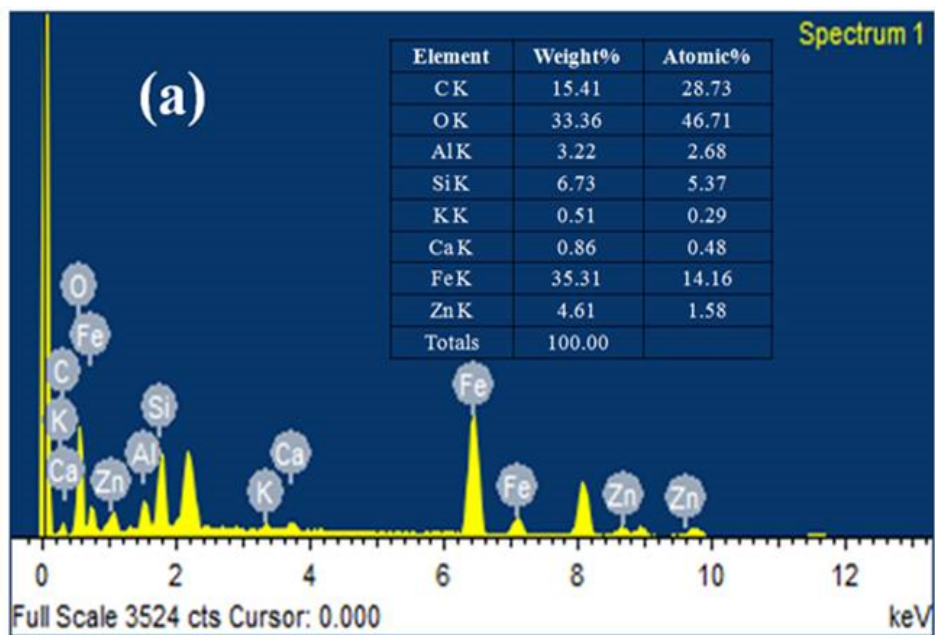
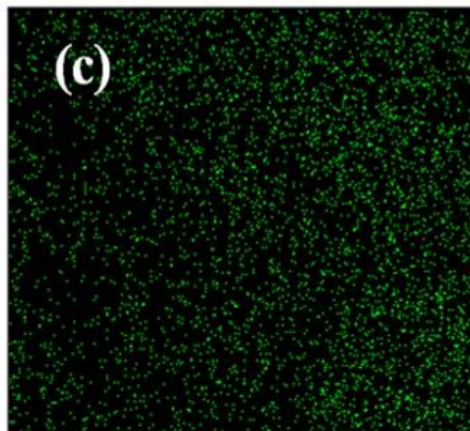


Figure 2

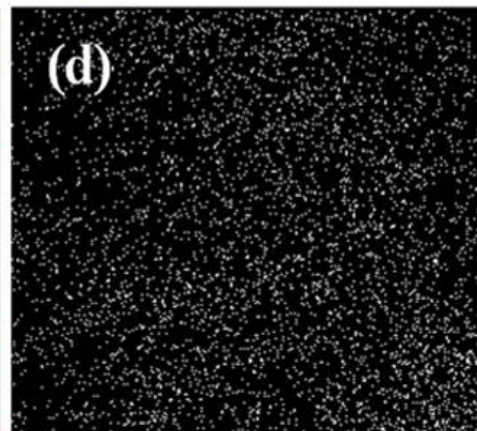
(a) EDX analysis and (b-d) Elemental Mapping of uncalcined iron rust.



Fe Ka1



O Ka1



Si Ka1

Figure 3

(a) EDX analysis and (b-d) Elemental Mapping of calcined iron rust

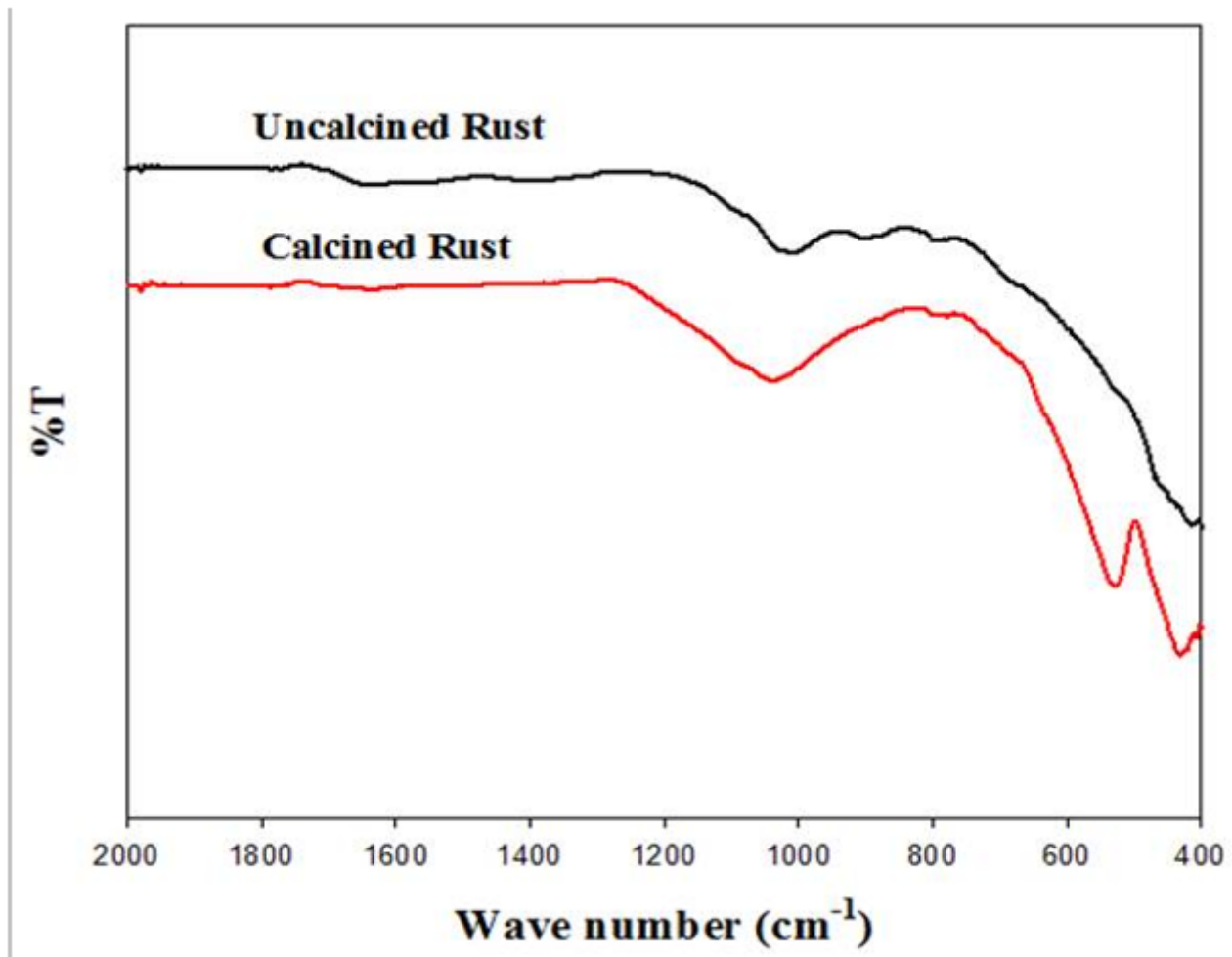


Figure 4

FTIR spectra of uncalcined and calcined iron rust

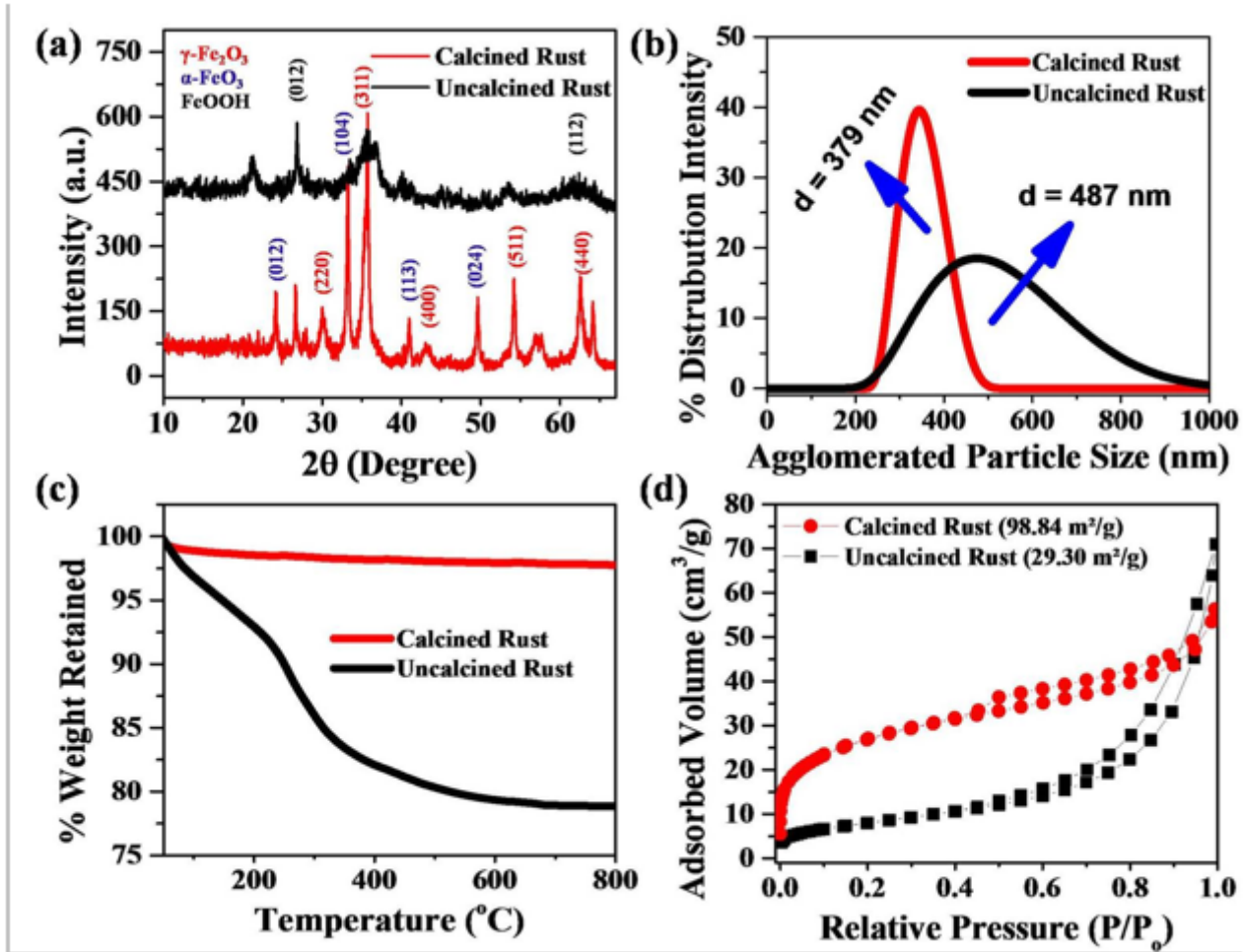
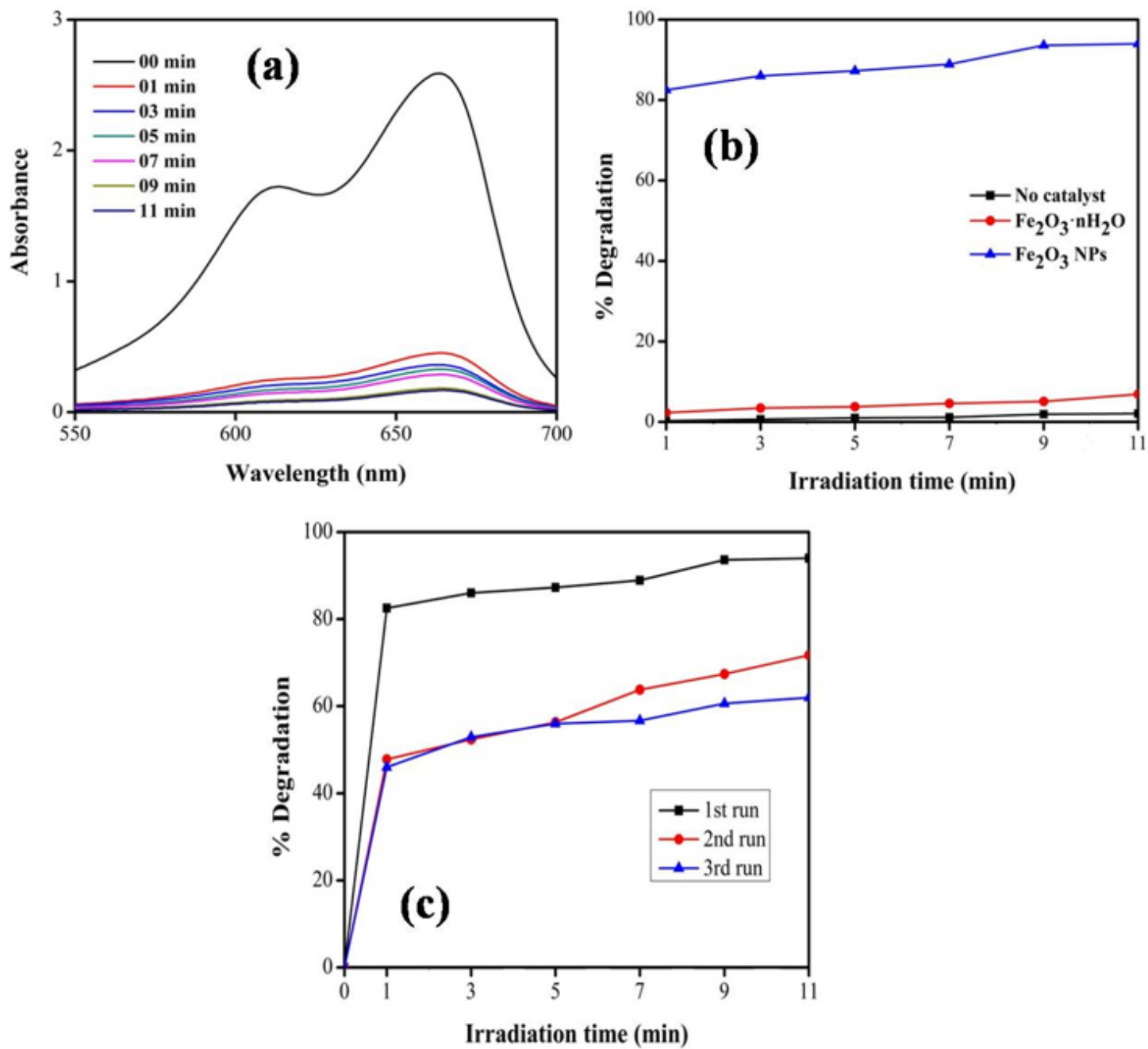


Figure 5

(a) XRD pattern (b) particle size distribution (c) Thermogravimetric analysis (d) BET surface area analysis of uncalcined and calcined iron rust.



**Figure 6**

(a) UV-Vis spectra of MB photodegraded by Fe<sub>2</sub>O<sub>3</sub> NPs in aqueous medium under visible light (b) %degradation comparison of MB dye photodegraded by Fe<sub>2</sub>O<sub>3</sub>·nH<sub>2</sub>O, Fe<sub>2</sub>O<sub>3</sub> NPs and without photocatalysts (c) reusability of Fe<sub>2</sub>O<sub>3</sub> NPs.

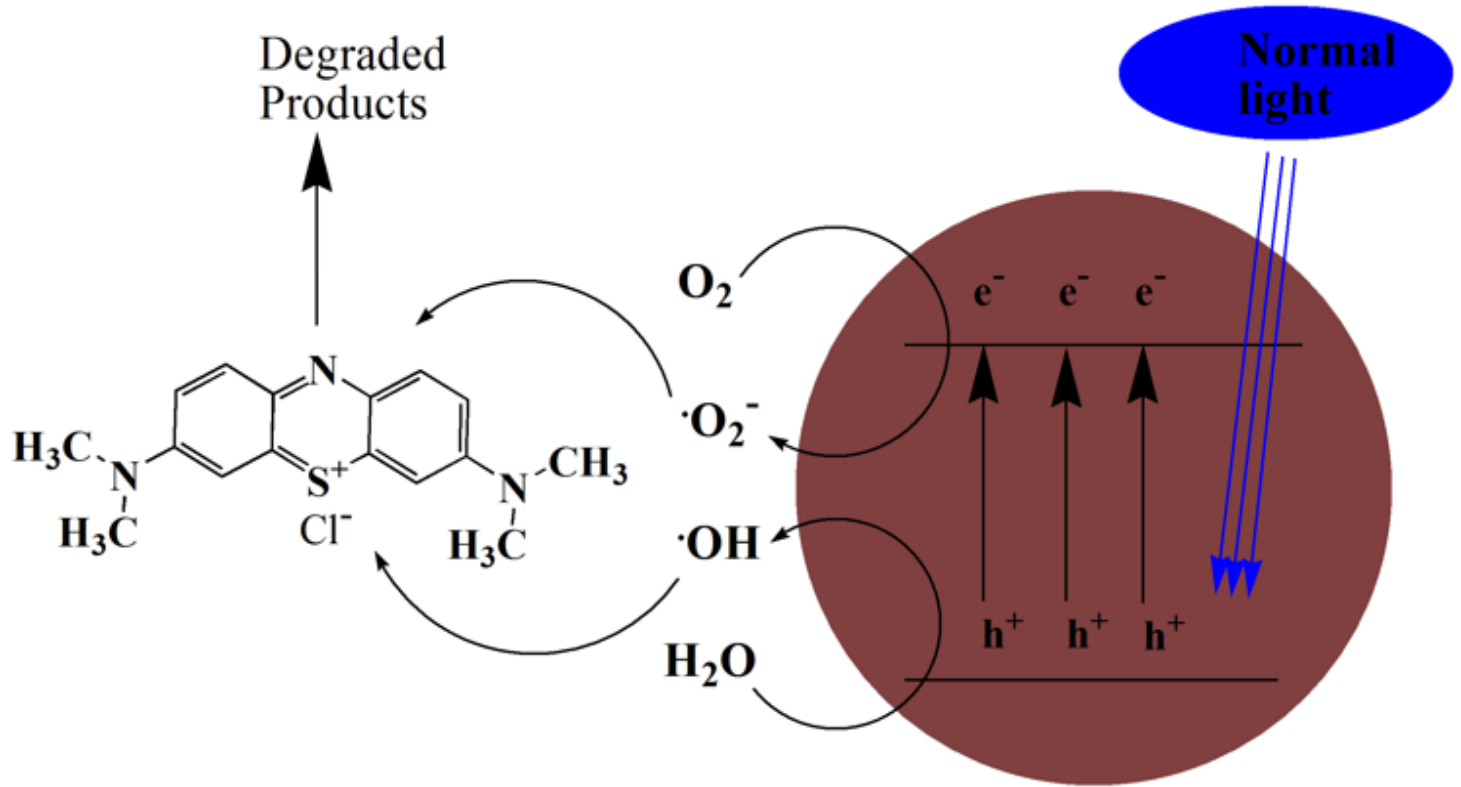
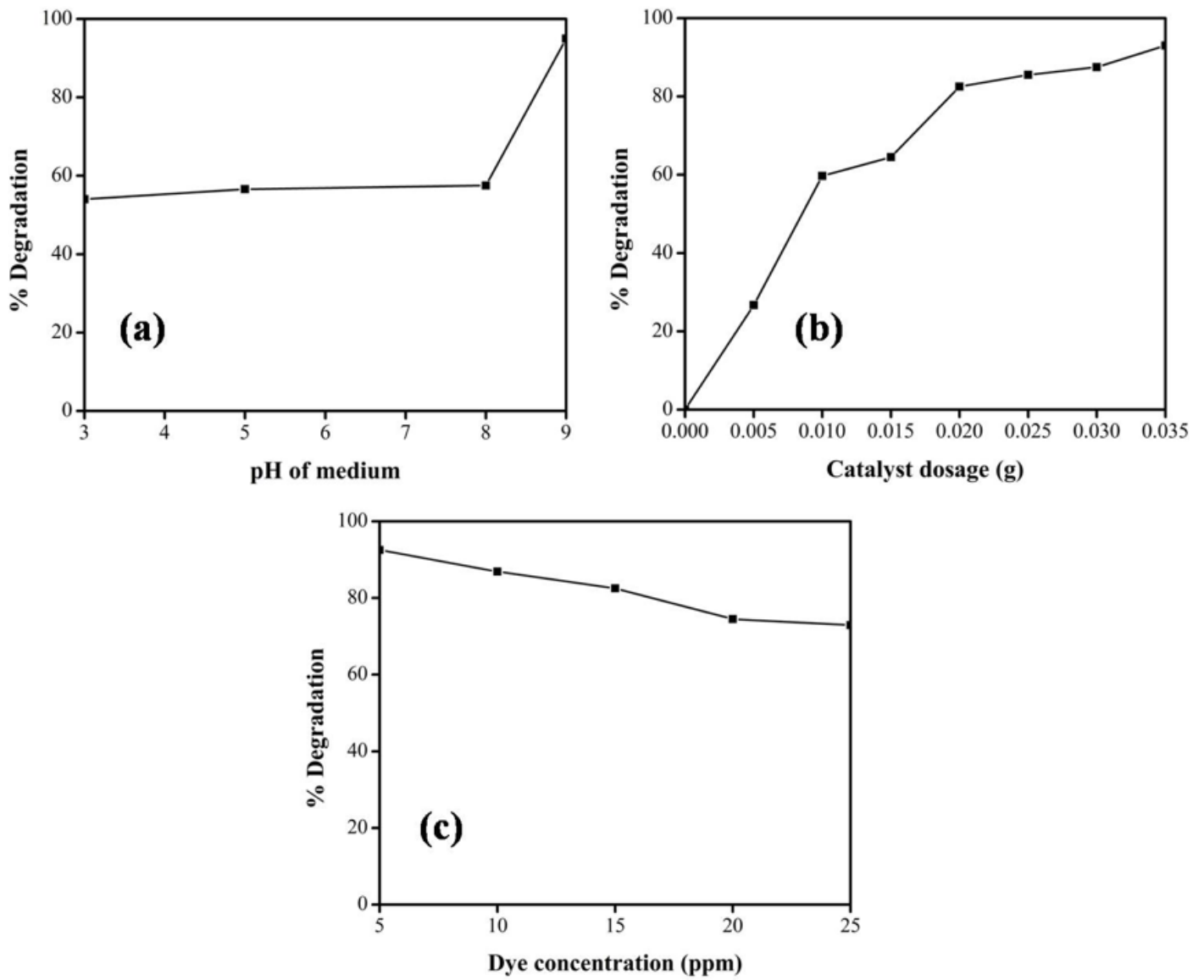


Figure 7

Proposed mechanism for the photodegradation of MB; adopted from (Khan et al. 2019).



**Figure 8**

(a) effect of pH of the medium on MB PD (b) effect of Fe<sub>2</sub>O<sub>3</sub> NPs dosage on MB PD (c) effect of the initial concentration of MB on PD of MB.

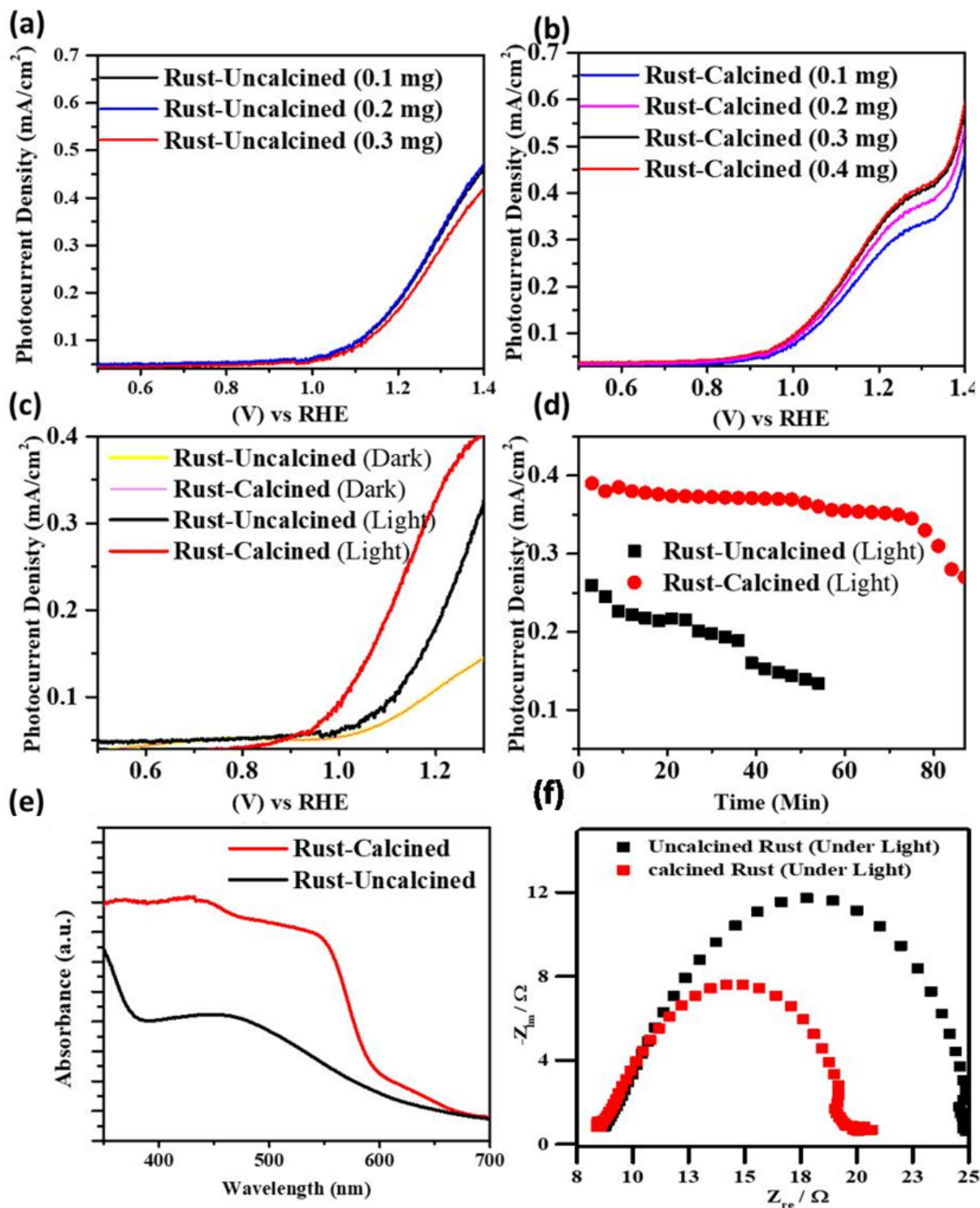


**Figure 9**

Photoelectrochemical measurements of Calcined and uncalcined Rust: (a,b) the catalytic dose-effect under visible light (c) Photoelectrochemical linear sweep voltammograms (d) chronoamperometric (I-t) stability curve (e) the UV/Vis-DRS absorption spectra, and (f) The EIS Nyquist plots.